Photocatalytic H_2 Evolution, CO_2 Reduction, and NO_x Oxidation by Highly Exfoliated g-C_3N_4

**Nadia Todorova [1],*, Ilias Papailias [1] , Tatiana Giannakopoulou [1], Nikolaos Ioannidis [1] ,
Nikos Boukos [1] , Panagiotis Dallas [1], Miroslava Edelmannová [2], Martin Reli [2] , Kamila Kočí [2],*
and Christos Trapalis [1]**

[1] Institute of Nanoscience and Nanotechnology, National Centre for Scientific Research "Demokritos",
15341 Athens, Greece; i.papailias@inn.demokritos.gr (I.P.); t.giannakopoulou@inn.demokritos.gr (T.G.);
n.ioannidis@inn.demokritos.gr (N.I.); n.boukos@inn.demokritos.gr (N.B.); p.dallas@inn.demokritos.gr (P.D.);
c.trapalis@inn.demokritos.gr (C.T.)

[2] Institute of Environmental Technology, VŠB-Technical University of Ostrava, 17. listopadu 15,
708 00 Ostrava-Poruba, Czech Republic; miroslava.edelmannova@vsb.cz (M.E.); martin.reli@vsb.cz (M.R.)

* Correspondence: n.todorova@inn.demokritos.gr (N.T.); kamila.koci@vsb.cz (K.K.);
Tel.: +30-210-650-3347 (N.T.); +420-597-327-309 (K.K.); Fax: +30-210-651-9430 (N.T.)

Abstract: g-C_3N_4, with specific surface area up to 513 m^2/g, was prepared via three successive thermal treatments at 550 °C in air with gradual precursor mass decrease. The obtained bulk and exfoliated (1ex, 2ex and 3ex) g-C_3N_4 were characterized and tested as photocatalysts for H_2 production, CO_2 reduction and NO_x oxidation. The exfoliated samples demonstrated graphene-like morphology with detached (2ex) and sponge-like framework (3ex) of layers. The surface area increased drastically from 20 m^2/g (bulk) to 513 m^2/g (3ex). The band gap (E_g) increased gradually from 2.70 to 3.04 eV. Superoxide radicals ($\cdot O_2^-$) were mainly formed under UV and visible light. In comparison to the bulk, the exfoliated g-C_3N_4 demonstrated significant increase in H_2 evolution (~6 times), CO_2 reduction (~3 times) and NO_x oxidation (~4 times) under UV light. Despite the E_g widening, the photocatalytic performance of the exfoliated g-C_3N_4 under visible light was improved too. The results were related to the large surface area and low e^--h^+ recombination. The highly exfoliated g-C_3N_4 demonstrated selectivity towards H_2 evolution reactions.

Keywords: g-C_3N_4 exfoliation; photocatalysis; H_2 evolution; CO_2 reduction; NO_x oxidation

1. Introduction

The increasing energy demand and the environmental pollution are two major problems that need to be resolved by the modern society. The photocatalytic technology is regarded as a potential solution because both hydrogen (H_2) production and air depollution (CO_2 reduction and oxidation of NO_x, VOCs, SO_x, etc.) can be achieved using abundant solar light [1].

For the photocatalytic H_2 production, water and various organic compounds have been used as sources. H_2 and O_2 have been produced by water splitting, while H_2, CO_2, and H_2O have been obtained by reforming of organic compounds under UV or visible light irradiation [2]. Modified TiO_2 and CdS are widely used as photocatalysts. Multicomponent systems including graphene, MoS_2, WO_3, etc. have also been constructed to create appropriate band gap configurations for light absorption and charge carriers (e^- and h^+) transportation [3]. Co-catalysts like Pt, Au, Ru/Rh, etc. are usually employed to enhance the efficiency of the main photocatalyst. Currently, g-C_3N_4 is intensively investigated as photocatalyst for H_2 evolution due to its visible light activation (band gap ~2.7 eV), suitable band gap potentials, stability, and low cost [4,5].

Regarding the photocatalytic CO_2 reduction, TiO_2 is the most commonly used photocatalyst but the application is still limited by its well-known drawbacks: the large band gap (~3.2 eV) and the fast recombination of the photo-generated charge carriers [6,7]. Other metal oxides (ZnO andCuO), sulfides (ZnS, CdS), carbides (SiC, MXenes), as well as their combinations have also been tested [8,9]. The g-C_3N_4 has been poorly investigated as a photocatalyst for CO_2 reduction and currently, it is receiving large research interest [10,11].For the photocatalytic NO_x oxidation and removal from the atmosphere, the TiO_2 and g-C_3N_4 are considered as most effective for operation under UV and visible light, respectively [12–14]. Due to their compatibility, the two photocatalysts have been coupled in different ratios achieving increased NO_x oxidation efficiency under visible light irradiation [15,16].

It is known that the performance of a semiconductor photocatalyst is dictated by energetic and morphological characteristics such as: (i) activation ability of the photocatalyst depending on the band gap energy (E_g), (ii) spontaneous involvement of the photogenerated e^- and h^+ in desired redox reactions governed by the valence and conduction bands potentials (V_{VB} and V_{CB}), and (iii) the mass transport and number of active sites depending on the porosity and the specific surface area (SSA). Although the use of g-C_3N_4 photocatalyst in the three cases of H_2 production, CO_2 reduction and NO_x oxidation is promising, it is inhibited by two main disadvantages, namely, the very low SSA (~10 m^2/g) and the high recombination rate of the photogenerated e^- and h^+ [17]. As a mitigation technique, exfoliation of the bulk g-C_3N_4 is carried out achieving ~10-fold increase of the SSA. Thermal and chemical routes have been employed with the latter to be more effective due to surface modification, enhanced superoxide radicals ($\cdot O_2^-$) formation, favorable band gap potentials, and porosity [18,19]. Nevertheless, the thermal route is often preferred due to the easy scale-up, low cost, and environmental friendliness. Thus, the two stages of g-C_3N_4 preparation, namely, synthesis of bulk g-C_3N_4 and its exfoliation via thermal treatment have been thoroughly investigated aiming at high yield and photocatalytic efficiency.

For the synthesis of g-C_3N_4, different precursor substances have been employed, such as triazines, dicyandiamide, thiourea, urea, melamine, etc., with the melamine to provide a relatively high yield of bulk g-C_3N_4 [20]. In addition, different experimental parameters have been tested such as: processing temperatures (450–650 °C), duration (1–3 h), exposure of the precursor (covered or non-covered), atmospheres (inert gas or air), presence of templates (e.g., SiO_2) and other substances (e.g., glyoxal), high pressure, etc. [21–23]. In the case of melamine precursor, treatment at 450 °C for 3 h in Ar atmosphere have been reported as optimum conditions with respect to photocatalytic performance of the g-C_3N_4 in NO_x oxidation [24]. The precursor quantity is another parameter that was found to greatly influence the properties of the synthesized g-C_3N_4. By decreasing the mass of the thiourea from 20 to 2 g, the SSA of the obtained g-C_3N_4 increased from 12 to 66 m^2/g and the NO removal rate increased from 12.7% to 48.3%. Mass-controlled synthesis, specifically "less is better" was proposed as a simple and facile strategy toward high-performance g-C_3N_4 photocatalyst [25].

Regarding the exfoliation, the bulk g-C_3N_4 is usually treated at similar thermal conditions resulting in approximately 6 to 10-fold increase of SSA. Intercalation of acidic substances prior treatment has been reported to cause an explosive exfoliation for only 3 min at 500 °C and to increase the SSA of the bulk g-$C_3N_4$from 9.6 to 58.9 m^2/g [26]. Following a different approach, repeated post-synthesis calcination of g-C_3N_4 was recently reported to increase the SSA and the photocatalytic NO removal and H_2 evolution. After seven successive calcinations, g-C_3N_4 nanosheets were prepared with improved crystallinity, SSA of 60 m^2/g, and rates of NO removal and H_2 evolution under visible light increased by factors of 1.74 and 24.4, respectively [27]. In addition, white g-C_3N_4 with SSA of ~265 m^2/g was prepared by applying thermal exfoliation twice at 550 °C [28]. It should be noted that in an earlier report [29], graphene-like g-C_4N_4 nanosheets with improved $\cdot$OH radical generation and H_2 evolution were obtained by a single thermal treatment of 400 mg bulk g-C_3N_4 at 500 °C for 2 h in static air. The measured SSA 306 m^2/g is among the highest reported but it was not connected to the mass of the treated bulk g-C_3N_4.

In this work, two variables, namely, the mass of the precursor and the number of exfoliations were combined applying three successive exfoliations with a gradual mass decrease. Highly exfoliated g-C$_3$N$_4$ with significant increase of the SSA up to 513 g/m^2 was achieved for the first time to the best of our knowledge. The prepared g-C$_3$N$_4$ materials were characterized and their photocatalytic activity in different photocatalytic processes, namely, H$_2$ evolution, CO$_2$ reduction and NO$_x$ oxidation, was investigated. Selectivity towards specific photocatalytic reactions was identified.

2. Results and Discussion

2.1. Physicochemical Properties of Highly Exfoliated g-C$_3$N$_4$

2.1.1. Crystalline Structure

The XRD patterns of the synthesized (bulk) and exfoliated (1ex, 2ex and 3ex) samples presented in Figure 1 are typical for g-C$_3$N$_4$. The characteristic (002) and (100) diffraction peaks are well defined for the bulk sample at 2θ of 27.6° and 13.0°, respectively. The (002) diffraction peak reflects the graphite-like stacking of g-C$_3$N$_4$ layers that consist of conjugated aromatic units. The interlayer distance was calculated applying the Bragg's law. For the bulk g-C$_3$N$_4$, the distance was found to be 0.323 nm (Table 1), whereas for the exfoliated samples, a gradual decrease to 0.320, 0.319 and 0.318 nm was recorded with the increase of the exfoliation number. This is in agreement with the literature [29] where the shift of 2θ to larger values is attributed to the denser nanosheets stacking caused by the thermal treatment. Additionally, the intensity of the (002) peak decreases for the samples 1ex and 2ex in comparison to the bulk indicating an increased disorder. For the sample 3ex, although shifted to larger 2θ, the diffraction peak (002) appears enhanced implying increased number of aligned layers and hence increased crystallinity. Similar result has been observed in the literature [27] where the increased crystallinity along with the reduced interlayer distance was reported to facilitate the transfer of the photo-generated electrons to the crystal surface and the formation of reactive oxygen species. After the photocatalytic activity test, the trends in the interlayer distance (d) and crystallinity were preserved as evidenced in the Supplementary Material Figure S1. A slight shift of the (002) peak to larger 2θ was observed for all samples. The **d** value for the bulk was not altered, whereas a very small decrease was found for the exfoliated 1ex, 2ex, and 3ex g-C$_3$N$_4$.

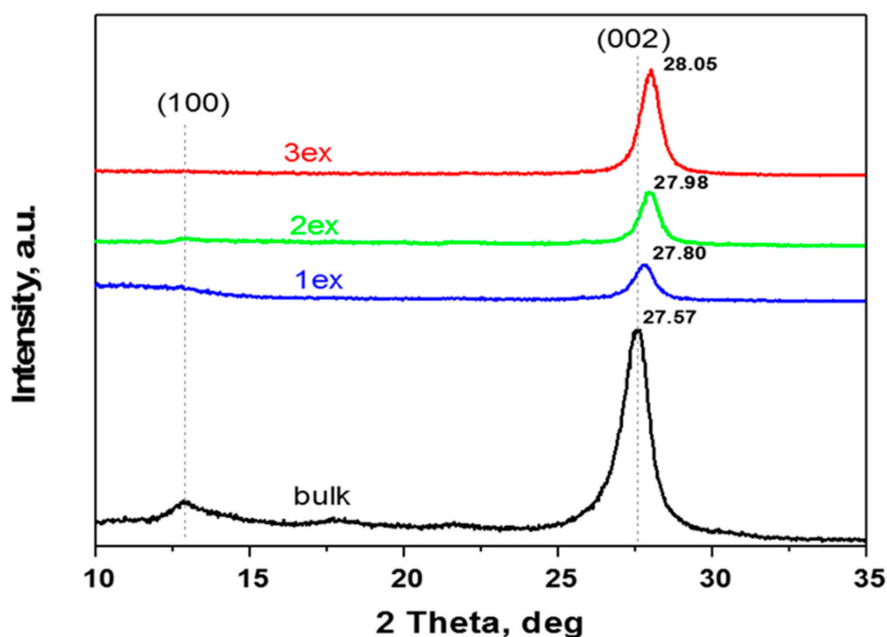**Figure 1.** Patterns of the synthesized (bulk) and exfoliated (1ex, 2ex and 3ex) g-C$_3$N$_4$.

Table 1. Distance (d), specific surface area (SSA_{BET}), total pore volume (V_p), main pore size (S_p), and pore size distribution.

Sample	d (nm)	SSA_{BET} (m²/g)	V_p (cm³/g)	S_p (nm)	Pore Size Distribution
Bulk	0.323	20	0.141	2	Narrow
1ex	0.32	127	0.821	1.8	Narrow
2ex	0.319	208	0.582	1.6	Wide
3ex	0.318	513	1.952	1.7	Wide

Regarding the (100) diffraction peak, it can be observed that with the increase of the exfoliation number, the intensity of the peak decreases and for the sample 3ex, it is missing. Since this peak is related to the in-plane tri-s-triazine units [30], it can be deduced that the planar size of the g-C_3N_4 layers decreased significantly after the exfoliations.

2.1.2. Morphology

The morphology of the bulk and exfoliated g-C_3N_4 can be observed in the SEM images at Figure 2. The bulk sample showed typical for the g-C_3N_4 aggregates of flakes. The sample 1ex was less aggregated but similar to the bulk, while for the highly exfoliated samples detached layers (2ex) and even a sponge-like framework of interconnected pores (3ex) can be observed.
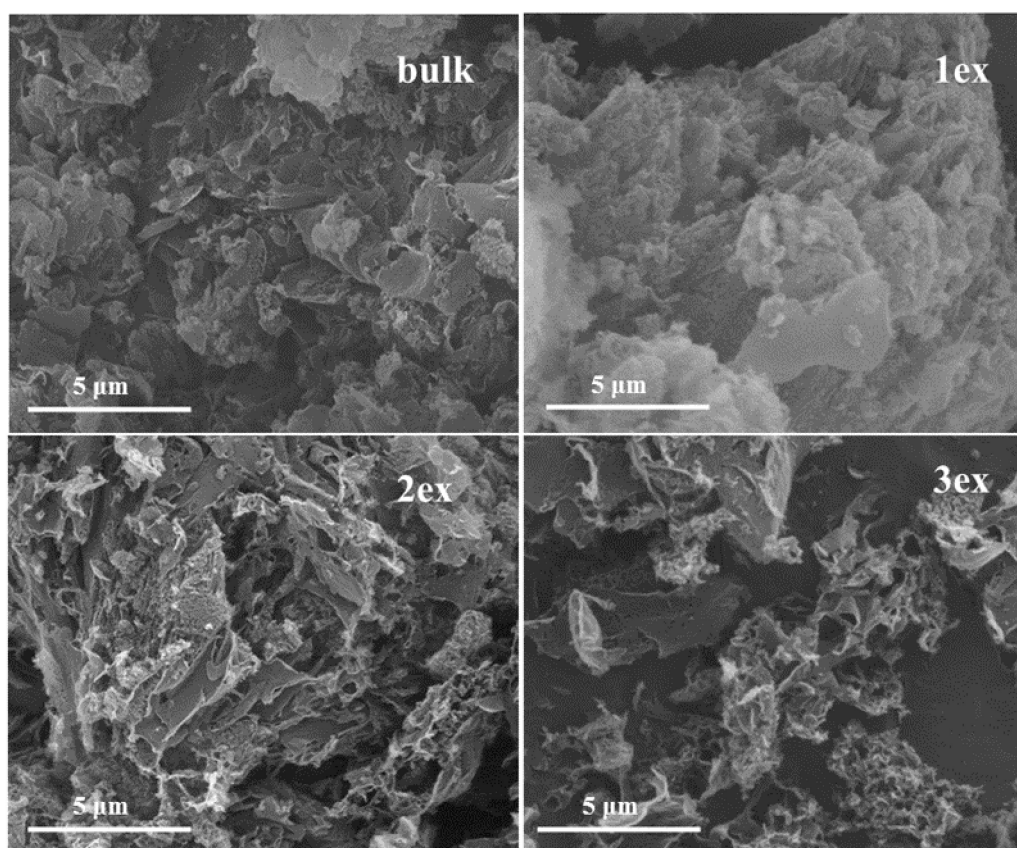

Figure 2. Images of the synthesized (bulk) and exfoliated (1ex, 2ex and 3ex) g-C_3N_4.

The TEM analysis of the exfoliated samples (Figure 3) evidenced a typical for 2D materials layered morphology. With the increase of the exfoliation cycles, the thickness of the stacked layers decreased (less dark color) indicating higher delamination. It can be expected that the thinner packs of g-C_3N_4 would facilitate the migration of the photogenerated e^- and h^+ to the surface where they will be engaged in redox reactions with species from the environment.
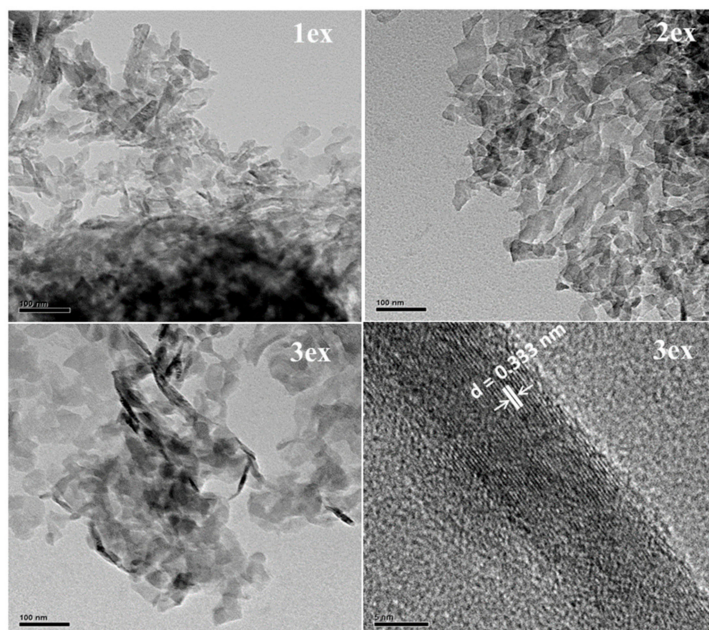
Figure 3. TEM images of the exfoliated (1ex, 2ex and 3ex) g-C_3N_4.

2.1.3. Porosity and Specific Surface Area

The liquid N_2 adsorption–desorption isotherms and the pore size distribution of the bulk and exfoliated g-C_3N_4 powders are given in Figure 4. According to Brunauer–Deming–Demin–Teller (BDDT) classification, the isotherms (Figure 4a) can be characterized as type IV suggesting multilayer adsorption and capillary condensation/evaporation. The shape of the hysteresis loops is consistent with type H3 of the Union of Pure and Applied Chemistry (IUPAC) classification indicating the presence of slit-shaped pores. It can be seen that the N_2 adsorption capacity of the exfoliated samples increased gradually in the entire range of the P/P$_0$. The total pore volume increased from 0.1413 cm^3/g for the bulk to 1.9520 cm^3/g for the 3ex sample (Table 1). In addition, the SSA determined by Brunauer–Emmet–Teller (BET) method increased drastically from 20 m^2/g for the bulk sample to 513 m^2/g for the 3ex sample. To our knowledge, this is the first time when g-C_3N_4 with so high SSA is reported in the literature.

The pore size distribution (Figure 4b) was determined from the desorption branch of the isotherm via Barrett–Joyner–Halenda (BJH) method. For the bulk g-C_3N_4, a narrow pore distribution was recorded with a well-defined peak at pore radius 2 nm and very small concentration of larger pores covering the wide range up to 100 nm. The sharp peak is assigned to the porosity within the g-C_3N_4 sheets, whereasthe large mesopores are ascribed to the voids between the packed layers [19,31]. After the first exfoliation (sample 1ex), the type of porosity was similar to the bulk with a slight shift of the main peak to smaller pore radius and increase of the concentration of the large mesopores. The second and the third exfoliation resulted in wider pore size distribution demonstrating a gradual increase of the pore sizes in both regions. This outcome is in good accordance with the results on the morphology of the bulk and exfoliated g-C_3N_4.

2.1.4. Chemical Composition

The FT-IR spectra of the bulk and exfoliated g-C_3N_4 presented in Figure 5 are rather similar. The absorption bands ascribed to g-C_3N_4 were preserved for all samples and became more prominent after the exfoliation treatments. The characteristic vibrations of N-H/O-N, C-N and s-triazine are well defined in the respective wavenumber regions as follows.

3000–3400 cm^{-1}: the broad bands near 3165 cm^{-1} are attributed to stretching vibrations of the N–H or O–H bonds of the residual amino groups or adsorbed H_2O molecules [25,32].
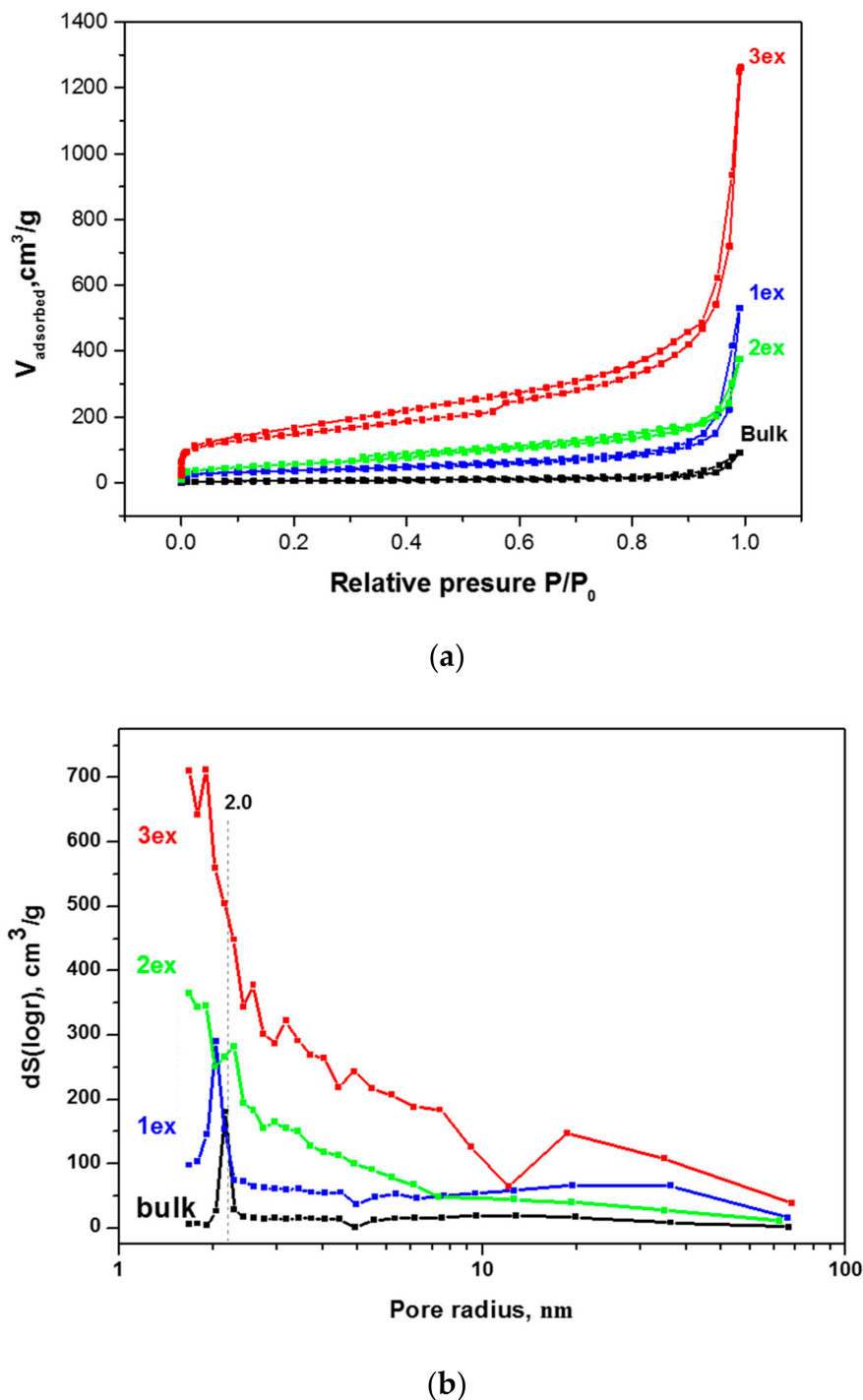
(**a**)

(**b**)

Figure 4. Liquid N_2 (nitrogen) adsorption–desorption isotherms (**a**) and pore size distribution (**b**) of the bulk and exfoliated g-C_3N_4.

1100–1700 cm^{-1}: the bands at 1230 cm^{-1} and 1313 cm^{-1} are associated with stretching vibrations of the C–N bonds between the heptazine rings and NH groups (or C–NH–C bridges), the bands at 1393, 1450, 1530 and 1626 cm^{-1} are connected to stretching vibrations of the C–N bonds in the rings [33,34].

700–900 cm^{-1}: the strong absorption at 805 cm^{-1} are ascribed to out-of-plane bending vibrations of the triazine/heptazine rings, the peak at 885 cm^{-1} is ascribed to deformation vibrations of the N–H bonds [35,36].

The comparison of the FT-IR spectra before and after their use in photocatalytic NO_x oxidation (Figure S2) demonstrated chemical stability of the prepared photocatalysts.
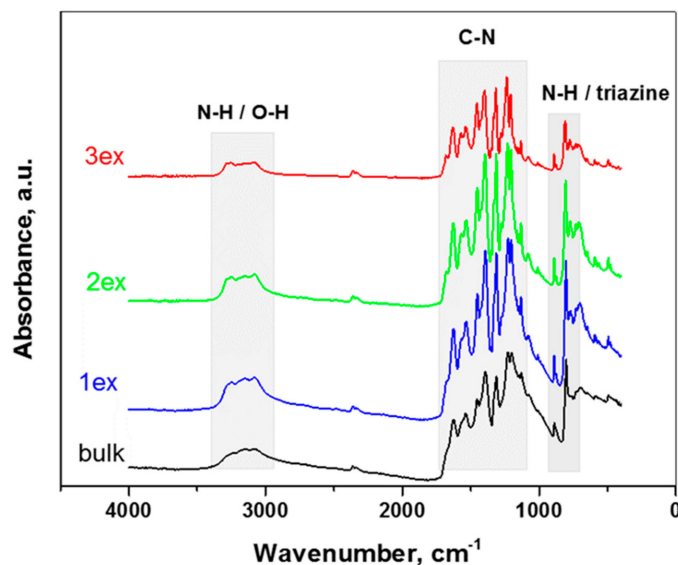
Figure 5. FT-IR spectra of the bulk and exfoliated (1ex, 2ex and 3ex) g-C$_3$N$_4$.

The surface and the total chemical composition determined by XPS and elemental analysis, respectively, are given in Table 2. It can be noted that the composition of all the samples is similar and their C/N atomic ratio ~0.63 is lower than the theoretical 0.75 for g-C$_3$N$_4$ attributed to remaining amino groups due to incomplete polycondensation [24].

Table 2. Composition determined by XPS and elemental analysis.

Sample	XPS			Elemental Analysis			
	C (at.%)	N (at.%)	O (at.%)	C (%)	N (%)	H (%)	Atomic Ratio C/N
Bulk	43.37	52.11	4.52	33.81	62.36	0.75	0.6325
1ex	44.14	52.23	3.62	34.2	63.25	0.77	0.6305
2ex	45.05	51.24	3.71	34.32	63.71	0.93	0.6286
3ex	44.31	51.22	4.46	34.63	62.41	0.8	0.648

2.1.5. Light Absorbance and Band Gap Characteristics

The diffuse reflectance spectra of the bulk and exfoliated g-C$_3$N$_4$ are depicted in Figure 6a. It can be seen that the reflectance increased with subsequent exfoliations that is consistent with the change of the color from yellow (bulk and 1ex) to white (2ex and 3ex) g-C$_3$N$_4$. In addition, the absorption edge and the main absorbance were shifted to lower wavelength. This phenomenon is known as blue shift and indicates an increase of the band gap energy (Eg) of the semiconductor.

Fluorescence spectroscopy measurements were carried out to evaluate the amount of photoexcited electrons and the radiative recombination degree of the photogenerated electron–hole pair. The observed shifts on the emission maxima (λ_{em}) of the samples (see inset of Figure 6a) are in good agreement with the blue shift of the absorption edge of the diffuse reflectance spectra. Specifically, the emission maxima shift from 460 nm for the bulk and the 1ex samples to 434 nm for the 2ex and 3ex. The 460 nm peak can be still seen as a shoulder in the highly exfoliated samples, implying a complex emission mechanism with two different dominant relaxations. The two different peaks are more prominent at the 1ex sample and became less pronounced as the exfoliation proceeded. In accordance to the lower reflectance of the exfoliated samples, their emission is also increased. In order to evaluate the photon emission of each sample, the fluorescence spectra were integrated for the emission range of 390–607 nm. The ratio of the area (denoted as A) between the samples and the bulk, which was used as reference, is: A$_{bulk}$:A$_{1ex}$ = 0.98, A$_{bulk}$:A$_{2ex}$ = 0.50, and A$_{bulk}$:A$_{3ex}$ = 0.55. It should be noted that the amount of the

2ex and 3ex samples necessary to fill the quartz holder was significantly lower compared to the 1ex and bulk samples. Nevertheless, the amount of emitted photons was significantly higher. This was assigned to the increased specific surface area and number of active centers.
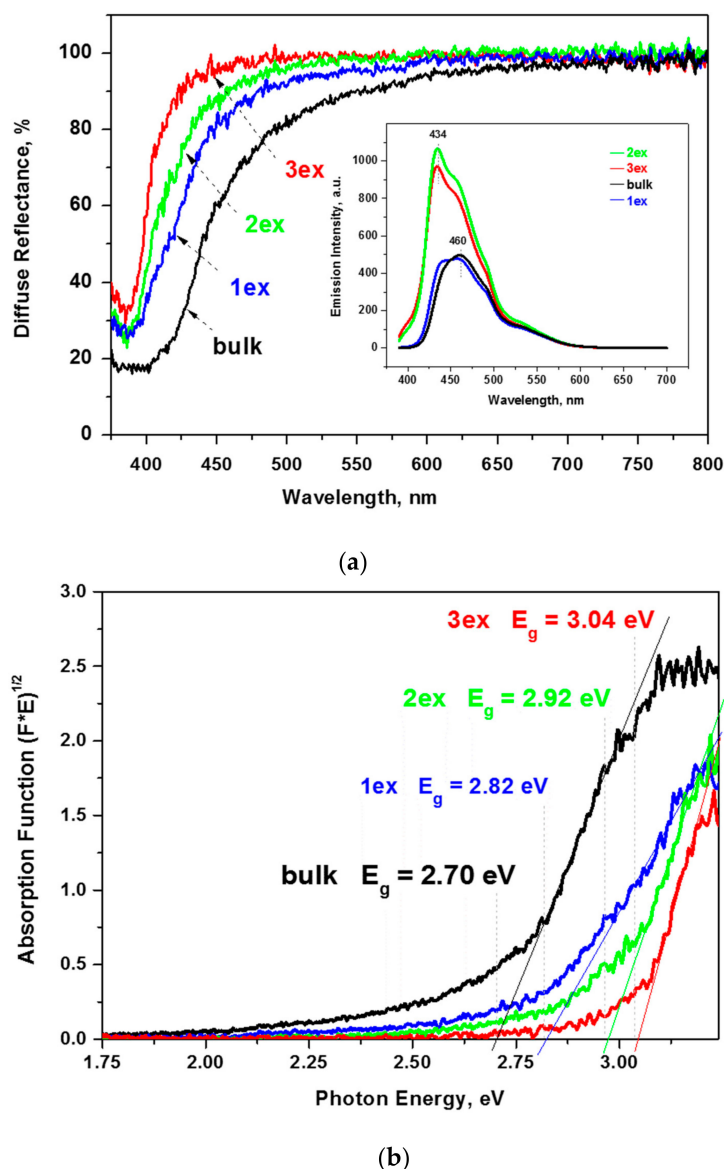

(a)

(b)

Figure 6. Reflectance spectra and photoluminescence (PL) emission spectra (inset) of the bulk and exfoliated g-C$_3$N$_4$ (**a**) and the respective absorption function plots (**b**).

The constructed plots from the diffuse reflectance absorption function $(E \times F)^{1/2} = f(E)$ and the linear extrapolation (Figure 6b) demonstrated a significant increase of the E$_g$ from 2.70 eV for the bulk to 3.04 eV for the 3ex g-C$_3$N$_4$. The outcome was related to the quantum confinement effect [19,37] due to the reduced thickness of the stacked layers in the highly exfoliated samples as revealed by the XRD and electron microscopy analyses. The activation of the exfoliated g-C$_3$N$_4$ with higher energy is expected to have a negative effect on the visible light response of the photocatalysts and competes the effect of the increased SSA and porosity.

The position of the band gap edges, namely, the conduction band (CB) and valence band (VB) potentials were determined through electrochemical measurements. In Figure 7a, the Mott–Schottky plots for one frequency (100 Hz) are displayed as measured versus Ag/AgCl electrode at pH 5.8.

The conduction band potentials (V_{CB}) were recalculated against normal hydrogen electrode (NHE) at pH 0 using the equation:

$$V_{CB} \sim V_{FB} \ (NHE; pH\ 0) = V_{FB} \ (Ag/AgCl, pH\ 5.8) + \Delta V + 0.059 \times 5.8,$$

where $\Delta V = 0.21$ V is the Ag/AgCl (3 M) potential against NHE. The valence band potentials (V_{VB}) were found using the equation:

$$V_{VB} = V_{CV} + Eg/e,$$

where **e** is the elementary charge. The values received are listed in Table 3 and schematically presented in Figure 7b.
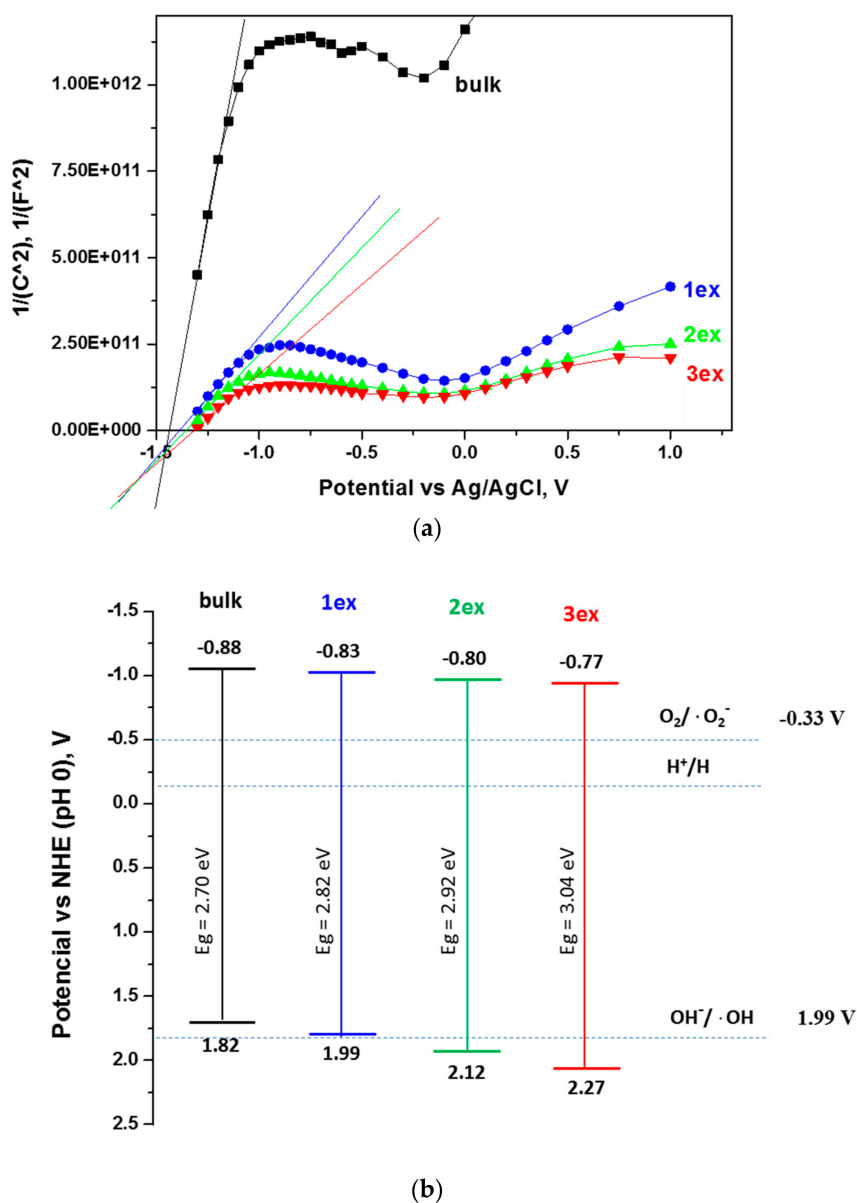

(a)

(b)

Figure 7. Mott–Schottky plots for frequency 100 Hz (**a**) and schematic presentation of the band gap potentials (**b**) of the bulk and exfoliated g-C_3N_4.

It is evident that the conduction band potentials were slightly shifted to less negative values from −0.88 V for bulk to −0.77 V for 3ex g-C_3N_4. Consequently, the distance between the V_{CB} and the O_2/O_2^- redox potential (−0.33V) was decreased meaning that the reductive power of the

photogenerated electrons was decreased and may affect the formation of superoxide ($\cdot O_2^-$) species. Nevertheless, the formation of $\cdot O_2^-$ species remains a spontaneous process since the required potential of -0.33 V was below the V_{CB}. The calculated valence band potentials increased from 1.82 V for bulk to 2.27 V for 3ex g-C_3N_4. The V_{VB} of the bulk and 1ex samples did not reach the redox potential of $OH^-/\cdot OH$ (1.99 V) indicating that the photogenerated holes cannot participate in the formation of $\cdot OH$. On the contrary, the V_{VB} of 2ex and 3ex are positioned below the 1.99 V meaning that the photogenerated holes can be engaged in $\cdot OH$ formation and the photocatalytic activity of these samples can be enhanced.

Table 3. Gap energy and potentials of the conduction and the valence bands.

| Sample	Band Gap E_g (eV)	Conduction Band Potential (V)		Valence Band Potential (V)
		vs. Ag/AgCl, pH 5.8	vs. NHE, pH 0	vs. NHE, pH 0
Bulk	2.70	−1.43	−0.88	1.82
1ex	2.82	−1.38	−0.83	1.99
2ex	2.92	−1.35	−0.80	2.12
3ex	3.04	−1.32	−0.77	2.27

2.2. Active Species Formation

Since the reactive oxygen species (ROS) such as hydroxyl and superoxide radicals are unstable species, their formation upon illumination is measured indirectly by trapping them with the nitrone DMPO (5,5-dimethylpyrroline-*N*-oxide) to stable, long-lived adducts, which are measurable by EPR (Electron Paramagnetic Resonance) [38,39]. From the EPR spectra of the bulk and exfoliated g-C_3N_4 (Figure 8a,b), it can be deduced that the successive exfoliation led to a gradual increase of the DMPO adducts under UV and visible light illumination. The identification of the formed ROS for the most active 3ex sample was performed by fitting of the experimental curves with simulated ones (Figure 8c,d). It was found that under UV light illumination, the majority of the formed ROS are superoxide radicals (95%), while the amounts of the hydroxyl (3%) and methoxy (2%) radicals were low. Under visible light, the amount of the superoxide radicals was also the dominant (68%), against the hydroxyl radicals (1%). The recorded amount of methoxy radicals $\cdot OCH_3$ was ascribed to the reaction of the created superoxide radicals with the acetonitrile from the systemas documented in the literature for various photocatalysts [40,41]. The observed dominance of the superoxide radicals against the hydroxyl radicals is in agreement with the results from the electrochemical analysis.
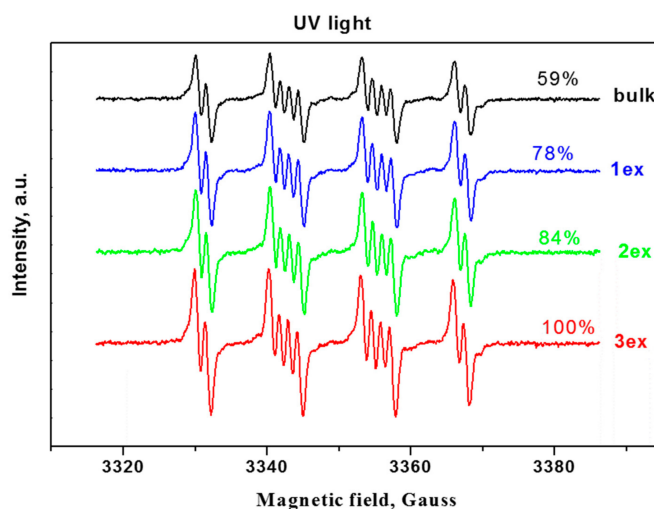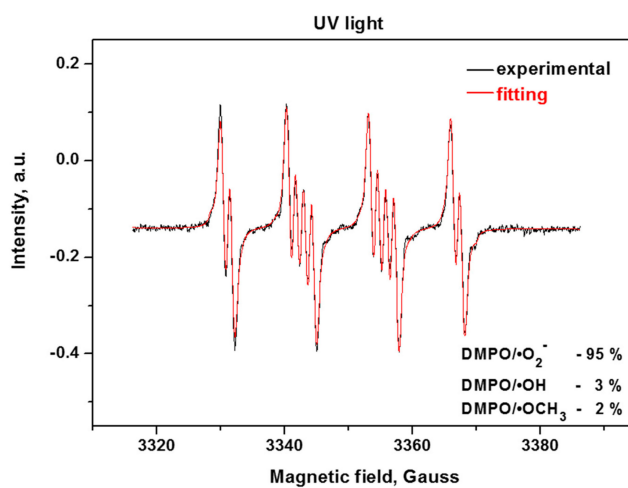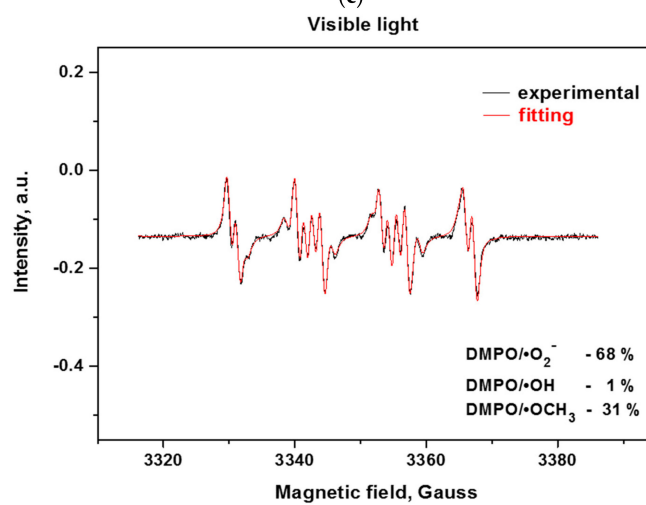

(a)

Figure 8. *Cont.*
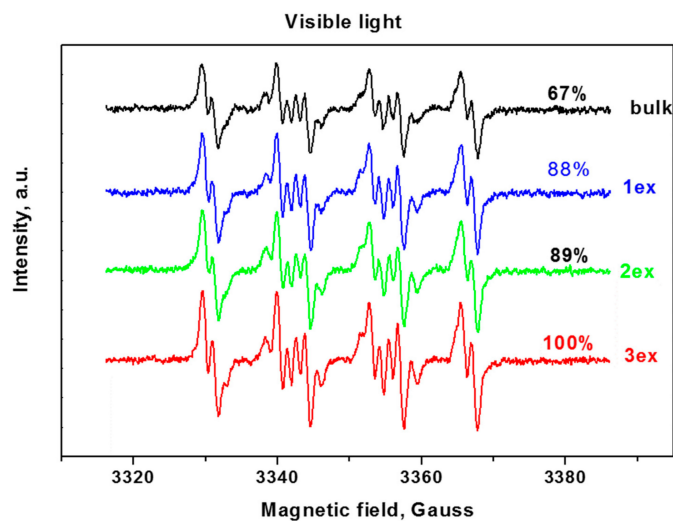
(**b**)

(**c**)

(**d**)

Figure 8. EPR spectra of radical adducts of DMPO under UV (**a**) and visible light (**b**) and simulation of radical adducts for sample 3ex under UV (**c**) and visible light (**d**).

Photocurrent measurements were conducted in order to estimate the amount of generated charge carriers in the photocatalysts (Figure 9). Although the amount of generated photocurrent does not reflect the photocatalytic activity of the measured photocatalyst, the results can provide a certain insight into the process itself. Since the photocurrent generation was measured in the presence of external potential applied to the working electrode, the generated electrons were "forced" to migrate to the ITO foil and the recombination of charge carriers was significantly suppressed. Therefore, the photocurrent generation can be used for the comparison of the amount of generated charge carriers (recombination is suppressed and electrons are measured in the form of current). For example, samples 1ex and 3ex provide similar photocurrent around 380 nm, however, their photocatalytic activity in photocatalytic hydrogen production and photocatalytic reduction of CO_2 is very different.
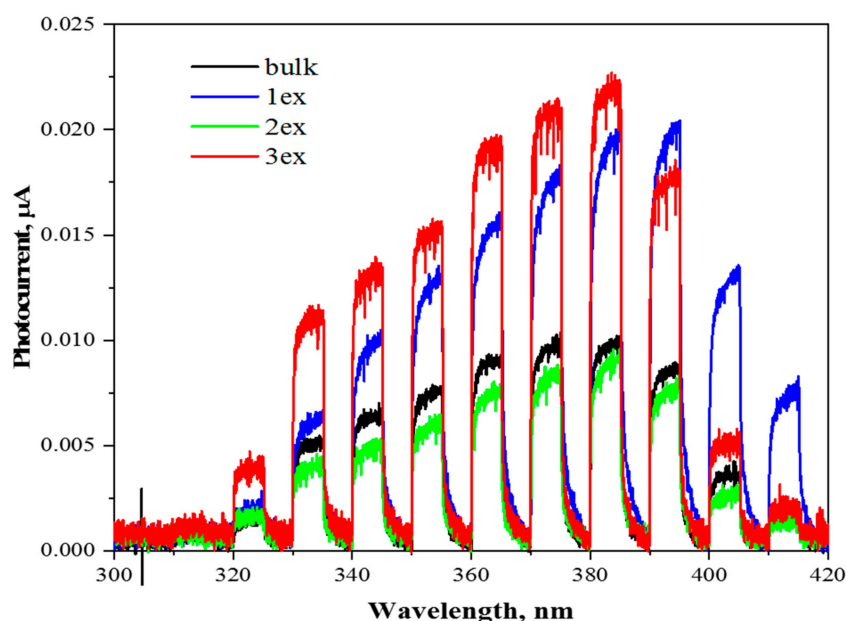

Figure 9. Photocurrent responses of the bulk and exfoliated (1ex, 2ex and 3ex) g-C_3N_4 under external potential of 1 V.

The results are pointing toward significantly improved charge separation in case of 3ex sample. Both samples, 1ex and 3ex, had approximately the same amount of charge carriers after irradiation, but much more electrons and holes were used for the reaction itself in case of 3ex sample.

2.3. Photocatalytic Activity

2.3.1. Photocatalytic H_2 Production

The experimental H_2 concentration curves recorded under UV and visible light are given in the Supplementary Material (Figure S3), whereas the calculated H_2 evolution rates of the samples in $\mu mol \cdot g^{-1} \cdot h^{-1}$ are presented in Figure 10. It can be noticed that the activity increased gradually with the increase of the exfoliation number. Under both UV and visible light, the exfoliated (1ex, 2ex and 3ex) g-C_3N_4 exhibited significant increase in H_2 evolution in comparison to the bulk. The increase was very prominent under UV light where the activity of the 3ex (343.81 $\mu mol \cdot g^{-1} \cdot h^{-1}$) was ~6 times higher than bulk (58.54 $\mu mol \cdot g^{-1} \cdot h^{-1}$) and ~3.7 times higher than the activity of 1ex (91.52 $\mu mol \cdot g^{-1} \cdot h^{-1}$). The significant increase of the H_2 evolution was attributed to the increased porosity and surface area that are important for the mass (reagents and products) transport and provided active sites for the redox reactions. The increased formation of the superoxide radicals correlates well with the recorded activity as well. According to the mechanism given in the literature [42,43], the sacrificial agent TEOA reacts with the photogenerated holes (h^+), while the photogenerated electrons (e^-) are transferred to the Pt sites where the H^+ are reduced to H_2. Under visible light, the H_2 evolution of 3ex reached the value

$35.86 \ \mu mol \cdot g^{-1} \cdot h^{-1}$ that is ~2 times higher than bulk ($18.23 \ \mu mol \cdot g^{-1} \cdot h^{-1}$). The lower impact of the exfoliation on the visible light activity is attributed to the limited light absorption due to widening of the band gap from 2.70 eV (bulk) to 3.04 eV (3ex). The activity of the exfoliated g-C_3N_4 under UV light did not reach the activity of the typical UV photocatalysts P25 ($541.05 \ \mu mol \cdot g^{-1} \cdot h^{-1}$), but overcome its activity ($28.98 \ \mu mol \cdot g^{-1} \cdot h^{-1}$) under visible light. It should be mentioned that despite the large band gap of P25, visible light activity has been reported [15,44,45] that can be related to its specific phase and element composition.
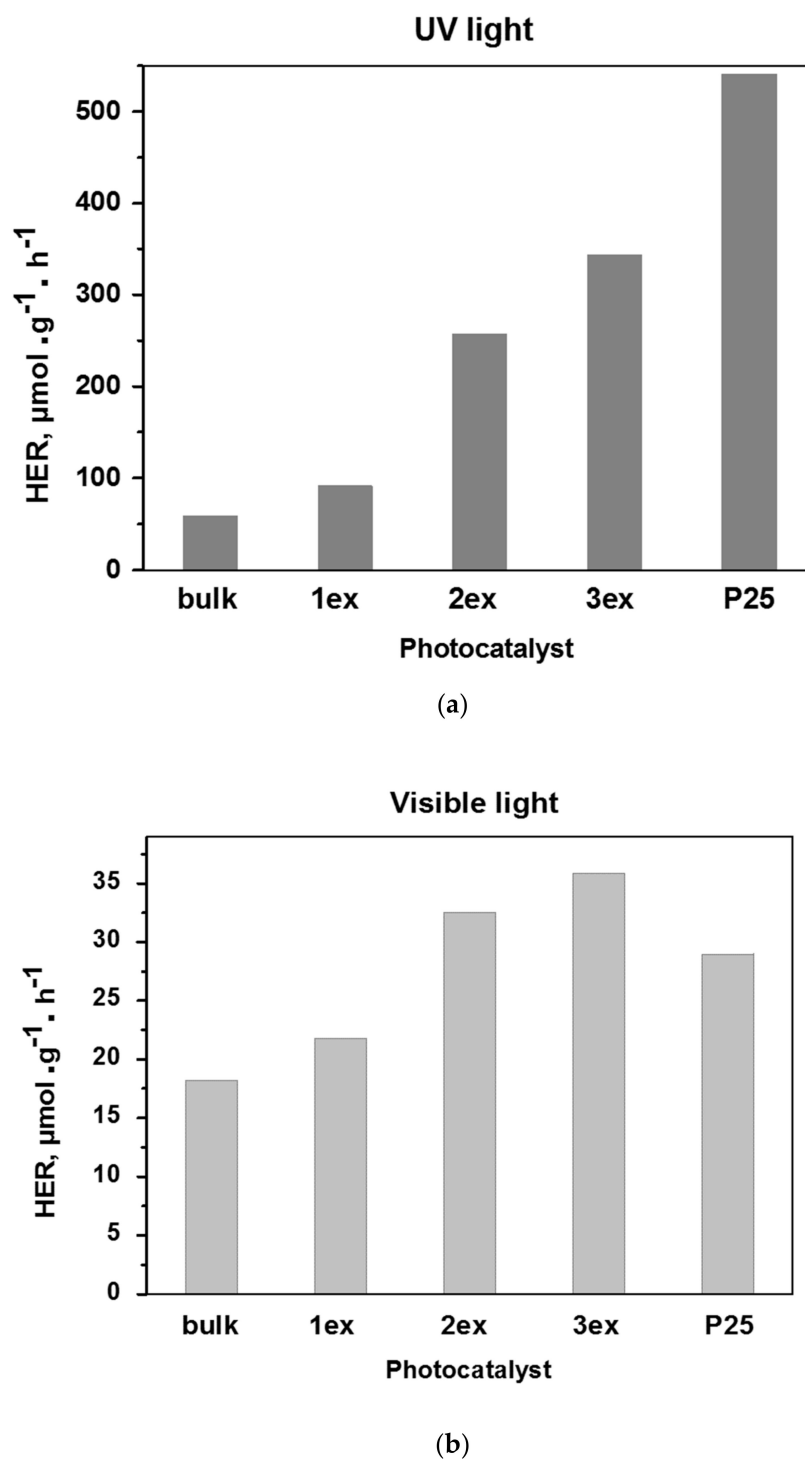

(**a**)

(**b**)

Figure 10. Photocatalytic activity of the g-C_3N_4 (bulk, 1ex, 2ex and 3ex) and P25 in H_2 evolution under UV (**a**) and visible (**b**) light.

2.3.2. Photocatalytic Reduction of CO_2

The main products of CO_2 photocatalytic reduction were methane and carbon monoxide, while the hydrogen formed from water splitting was also recorded [46,47]. The time dependence of product yields in presence of the investigated photocatalysts is shown in the Supplementary Material (Figure S4). The sum of all products (methane, carbon monoxide and hydrogen) yields over the photocatalysts after 8 h of irradiation is depicted in Figure 11. The photocatalytic activities of the photocatalysts followed the order 3ex g-C_3N_4>> 2ex g-C_3N_4> 1ex g-C_3N_4 ~ bulk g-C_3N_4. The yields of CH_4, CO and H_2 in presence of 3ex g-C_3N_4 photocatalyst were almost 3, 2 and 8 times higher, respectively, then in case of bulk g-C_3N_4 photocatalyst, whereas the lowest yield of H_2 and no yields of CH_4 and CO were observed in presence of the P25 photocatalyst. The significantly increased products' yields were ascribed to the exfoliation of the g-C_3N_4.
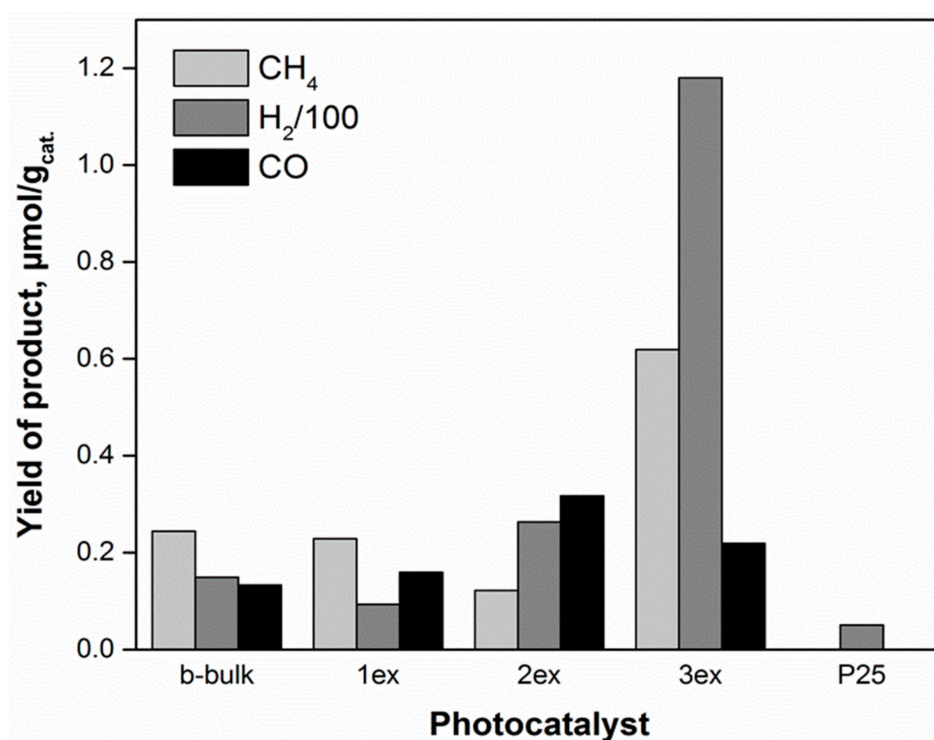

Figure 11. All product yields of CO_2 photocatalytic reduction (after 8 irradiation hours) over the g-C_3N_4 (bulk and 1ex, 2ex and 3ex) and P25 photocatalysts.
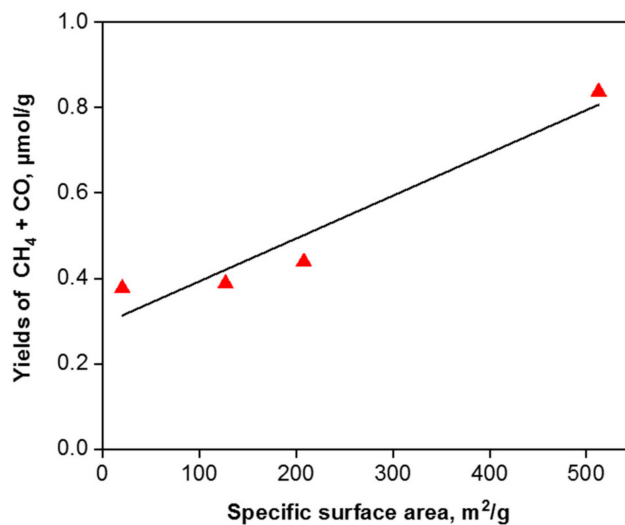
The correlation between the specific surface area and methane and carbon monoxide yields is depicted in Figure 12a.

The rate of electron consumption for the formation of reaction products was calculated according to the equation:

$$R(\text{electron}) = 8r(CH_4) + 2r(CO) + 2r(H_2)$$

where $r(CH_4)$, $r(CO)$ and $r(H_2)$ are the rates of CH_4, CO and H_2, respectively [8]. The correlation of the photogenerated electrons' efficiency with the specific surface area is shown in Figure 12b. Due to the fact that the CO_2 photocatalytic reduction to carbon monoxide and methane is competitive with the photocatalytic water splitting to hydrogen, the selectivity for CO_2 photocatalytic reduction was computed according to the equation [8]:

$$\text{Selectivity for } CO_2 \text{ reduction } (\%) = \frac{[2r(CO) + 8r(CH4)]}{[2r(CO) + 8r(CH4) + 2r(H2)]} \cdot 100\%$$

(**a**)
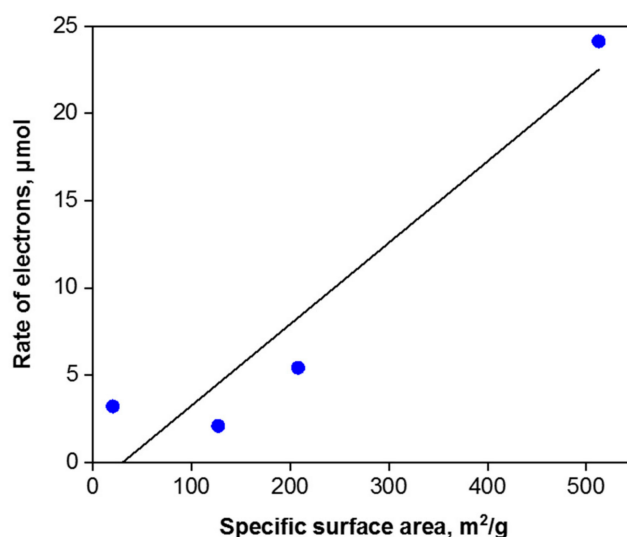
(**b**)

Figure 12. Correlation between the specific surface area and the yields of CH_4 and CO (**a**) and the rate of electron (**b**) in presence of g-C_3N_4 photocatalysts.

The correlation between the proportion of methane and carbon monoxide yield and selectivity for CO_2 photocatalytic reduction in presence of g-C_3N_4 photocatalysts is shown in Figure 13. It is evident that the exfoliation leads to higher selectivity for photocatalytic water splitting that is in agreement with the recorded high hydrogen evolution in Figure 10. The exfoliation of g-C_3N_4 accelerated the rate of electron consumption for reductive reactions, i.e., R(electron). In addition, the valence band potentials of the highly exfoliated samples (2ex and 3ex) facilitate the holes trapping and charge separation. Consequently, more electrons are present on the surface of the photocatalyst, which can react with CO_2 and H_2O to form CH_4, CO and H_2. The exfoliated g-C_3N_4 acted as efficient photocatalyst, which influences the efficiency of the reaction (higher yields of all products) as well as the selectivity towards the product formation.
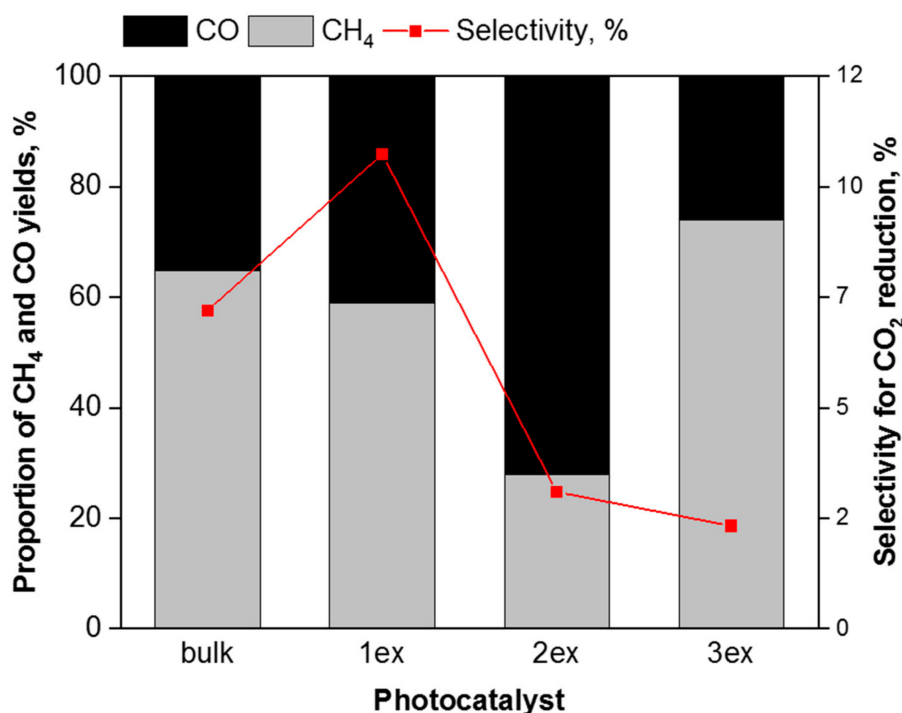
Figure 13. Correlation between the proportion of CO, CH_4 and H_2 yields and selectivity for the CO_2 photocatalytic reduction (after 8 irradiation hours) over the g-C_3N_4 photocatalysts.

2.3.3. Photocatalytic Oxidation of NO_x

The photocatalytic activity in oxidation of NO_x is estimated by: (i) the decrease of an initial NO concentration of 1 ppm, (ii) the increase of the formed NO_2 and (iii) the decrease of the total NO_x ($NO + NO_2$) concentration in the gas flow above the photocatalyst. The experimental concentration curves of NO, NO_2 and NO_x gases under UV and visible light irradiation of the bulk and exfoliated g-C_3N_4 are given in the Supplementary Material (Figure S5), whereas the calculated according to [48] efficiencies are presented in Figure 14. The respective data for the reference P25 photocatalysts is also presented. A gradual increase in NO oxidation (decrease of NO concentration), NO_2 formation and the total NO_x removal was demonstrated for the bulk, 1ex and 2ex samples, where the activity of 2ex was higher than that of 3ex.

The increase was more prominent under UV light where the total NO_x removal by 2ex and 3ex were ~4 and ~3 times higher than bulk, respectively. Under visible light, the efficiency of 1ex and 2ex in NO_x removal was almost 2 times higher than bulk, but the activity of 3ex was comparable to the bulk. When compared to P25, the 2ex g-C_3N_4 exhibited better activity in total NO_x removal under UV light and similar activity under visible light. The long-term (8 h) photocatalytic behavior of 2ex appeared very stable without indication for saturation or deactivation of the photocatalyst (Figure S6). Overall, the increase in NOx oxidation after the exfoliations was not analogous to the increase of the SSA. The outcome was related to the competition between the band gap parameters (E_g, V_{VB} and V_{CB}) and the specific surface area of the photocatalysts, as well as to the mechanism of the NO_x oxidation process. Despite the widening of the band gap from 2.70 eV (bulk) to 3.04 eV (3ex), the activity under both UV and visible light did not decrease, which can be ascribed to the drastic increase of the SSA of the exfoliated samples. Yet, despite the high SSA of 3ex (513 m^2/g), this sample displayed lower activity than 2ex (208 m^2/g) under both UV and visible light, suggesting that the SSA was no longer the dominant factor for the NO_x oxidation process. The fact that the produced reactive species were mostly superoxide radicals also explained the relatively low increase of the photocatalytic activity since the hydroxyl radicals played very important role in the mechanism of photocatalytic NO_x oxidation [49,50].

UV light

(**a**)
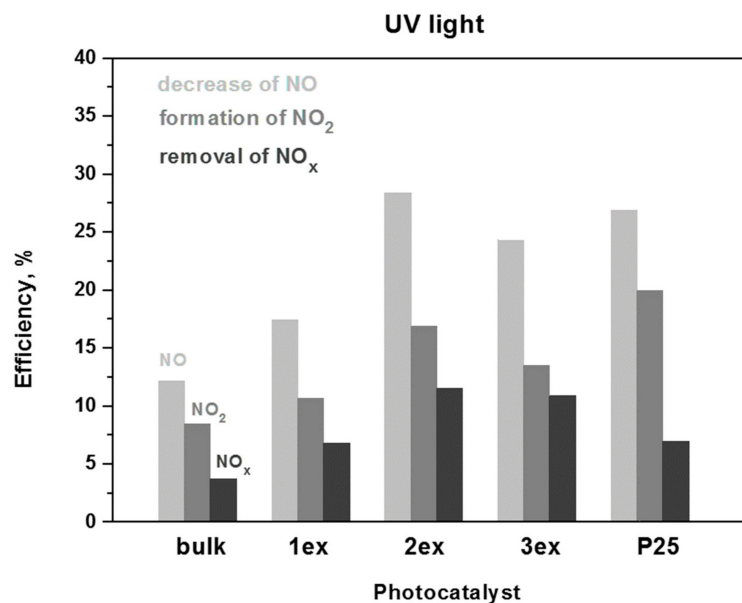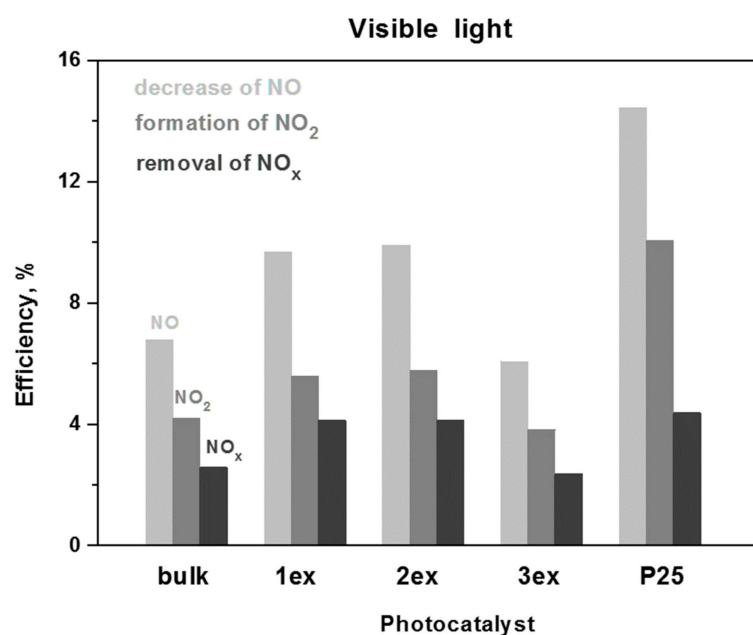
Visible light

(**b**)

Figure 14. Efficiency of the g-C_3N_4 (bulk, 1ex, 2ex and 3ex) and P25 in NO oxidation and NO_x removal under UV (**a**) and visible light (**b**) irradiation.

3. Materials and Methods

3.1. Sample Preparation

g-C_3N_4 powder was synthesized by thermal polycondensation of melamine $C_3N_6H_6$ in air atmosphere. Specifically, 20 g of melamine (Alfa Aesar) were placed in a beaker-shaped alumina crucible and heated up to 550 °C in a muffle furnace Carbolite CWF 1100 with heating rate 10 °C/min. The precursor material was treated non-covered for 3 h and cooled to room temperature naturally. Notably, 9 g of powder with characteristic yellow color was obtained (yield 45%) and nominated as sample bulk.

The exfoliation of the bulk powder was carried out at the same treatment conditions (non-covered, 550 °C, 3 h, in air). Multiple exfoliations were performed employing different quantities of the precursor material. Specifically, 2 g of the bulk material was used for the first exfoliation giving light yellow powder that was named 1ex. Then, 1g of 1ex powder was subjected to thermal treatment giving almost white fine powder that was denoted as 2ex. Finally, 0.5 g of 2ex material was treated giving white, free standing foam-like material 3ex. The preparation procedure with the corresponding yields and a comparative photograph of the obtained materials with equal quantity 0.030 g of each sample are shown in Figure 15. It should be mentioned that fourth treatment was performed using 0.25 g and 0.5 g of 3ex, but it resulted in total decomposition of the 3ex material.
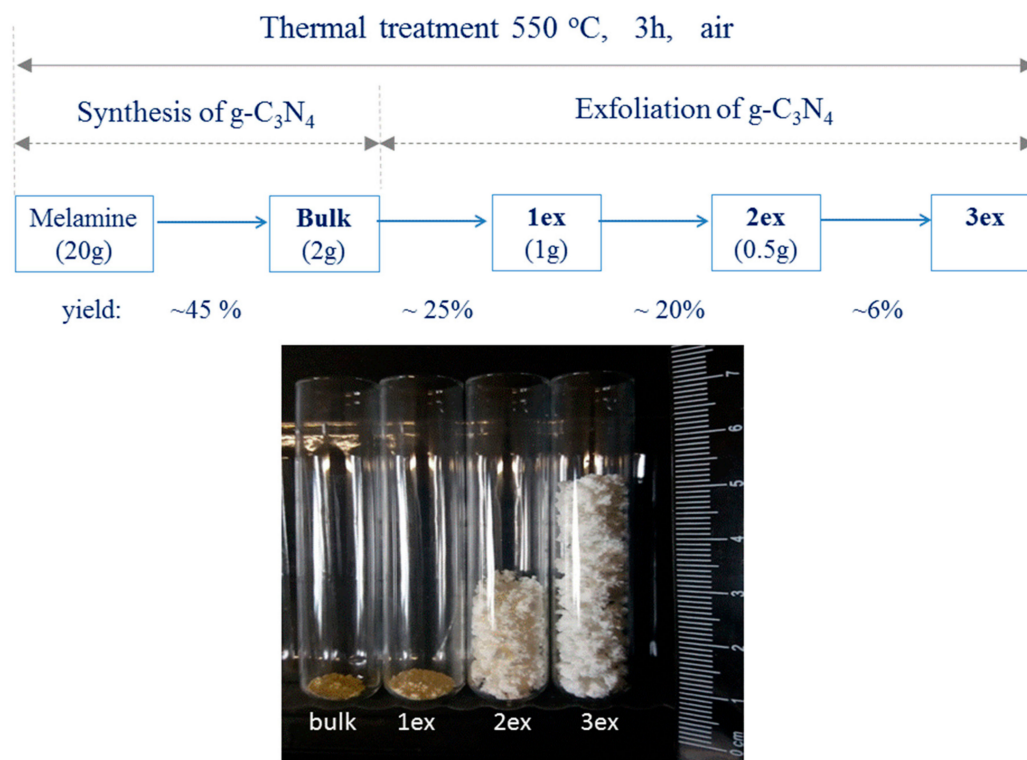

Figure 15. Schematic presentation of samples' preparation where the precursor mass in gram and the yield of each treatment in percent are given; photograph of equal quantity 0.030 g of the bulk and exfoliated (1ex, 2ex and 3ex) g-C_3N_4.

3.2. Characterization

The physicochemical properties of the prepared materials such as crystalline structure, morphology, porosity and specific surface area, surface chemical composition, and light absorption were investigated employing the respective analytical methods and techniques. Specifically, the XRD measurements were performed using a Siemens D500 X-ray diffractometer with a Cu Ka radiation source. SEM and TEM analysis were performed using a FEI Quanta Inspect and a FEI CM20 Microscope, respectively. The liquid N_2 adsorption–desorption isotherms were obtained with a Quantachrome Autosorb-iQ instrument. Prior to the measurement, the samples were degassed at 150 °C for 6 h. The FT-IR transmittance spectra of the materials were measured on a Nicolet iS50 FT-IR instrument. Elemental analysis was performed with a Perkin Elmer 2400 CHN analyzer. X-ray photoelectron spectroscopy was conducted with an ultrahigh vacuum VG EXCALAB 210 electron spectrometer using Mg Kα as radiation source. The UV–VIS diffuse reflectance spectra were recorded on a Shimadzu UV–2100 spectrophotometer using BaSO$_4$ as reference. The photoluminescence (PL) spectra were measured on a Jasco FP−8300 spectrofluorometer. Prior to the measurements, the excitation-dependent photoluminescence mapping was conducted in order to determine the adequate excitation wavelength.

Subsequently, the spectra were recorded under λ_{exc} = 370 nm. The diameter of the holder window was 18 mm. The mass of the bulk and 1ex samples was 86 mg, while the mass of the 2ex and 3ex was 16 mg due to the large volume of the latter.

The conduction band edge potential of the investigated materials was determined via Electrochemical Impedance Spectroscopy applying the Mott–Schottky (MS) approximation. The electrochemical measurements were performed employing a MetrohmAutolab PGSTAT302 potentiometer equipped with a beaker-type three-electrode cell. The exact methodology and the experimental parameters are thoroughly described in our previous work [51].

The formation of reactive oxygen species (ROS) by the g-C_3N_4 materials under UV and visible light irradiation was investigated employing a method for scavenging the short-lived ROS using the nitrone DMPO as a spin trap. The EPR measurements were performed using an extensively upgraded Bruker ER−200D spectrometer equipped with an Oxford ESR 900 cryostat, an Anritsu MF76A frequency counter and a Bruker 035M NMR gauss meter. The exact methodology and experimental parameters are described in our previous work [19].

Photocurrent measurements were conducted in classical three electrode system where saturated Ag/AgCl and Pt wire were used as reference and counter electrodes, respectively. The working electrode was prepared by depositing photocatalyst powder onto the conductive side of ITO (indium-tin oxide) foil. For that purpose, 0.1 M KNO_3 solution was used as electrolyte. Photocurrent action spectra were recorded using photoelectric spectrometer (Instytut Fotonowy, Poland) coupled with 150 W xenon lamp, monochromator, and potentiostat. The range of applied external potential was from −0.2 to 1.0 V (step 0.1 V) and the wavelength range was from 240 to 440 nm (step 10 nm).

3.3. Photocatalytic Activity Evaluation

The photocatalytic activity of the materials towards H_2 production, CO_2 reduction and NO_x oxidation under UV and visible light irradiation was investigated using the respective reactors and setups.

3.3.1. Photocatalytic H_2 Evolution

A homemade flow-type glass reactor with a quartz window was employed that was connected to a GC−2010 Shimadzu gas chromatograph equipped with a BID−2010 detector. Triethanolamine (TEOA) was used as sacrificial agent. Pt co-catalyst (3 wt%) was photodeposited using H_2PtCl_6 precursor. Briefly, 0.030 g of each sample were dispersed in 50 mL 10 vol% aqueous solution of TEOA where the required amount of H_2PtCl_6 was added. The mixture was transferred to the reactor, sealed with the quartz window and purged with Ar (10 mL/min) to remove the dissolved oxygen and the residual air. The Pt co-catalyst was deposited by irradiation of the dispersion for 30 min under stirring. Then, the concentration of the H_2 gas (ppm) was measured with a GC−2010 Shimadzu gas chromatograph equipped with a BID−2010 detector in intervals of 10 min until stabilization and the final H_2 evolution rate ($\mu mol \cdot g^{-1} \cdot h^{-1}$) was calculated. Philips CLEO15W Compact lamps and Osram 400 W R7S lamp (spectrum at Figure S7) were used to produce UV-A and visible light irradiation with intensity of 6.3 W/m^2 and 35000 lx, respectively.

3.3.2. Photocatalytic CO_2 Reduction

For the CO_2 reduction measurements, a homemade batch-type stainless-steel reactor with a quartz window was employed. Ultra-Violet Products Inc. Hg lamp 8 W with peak intensity at 365 nm was used as a light source that was located above the quartz window. Precisely, 0.090 g of each sample was dispersed in 100 mL 0.2 M aqueous solution of NaOH that was transferred to the reactor, sealed and purged with He or CO_2. Pressure sensor Greisinger, GMSD 3,5 BAE was placed at the top of the reactor to control the experiment. The suspension was kept under stirring all the time to prevent the settling of photocatalyst. The gaseous samples were analyzed within the time interval 0–8 h, where 0 means before the switching on the UV lamp. The samples were randomly taken with a gastight

syringe (Hamilton Co., Reno, NV, USA) to the gas chromatograph (Shimadzu Tracera GC−2010Plus) equipped with BID (barrier discharge detector). Each photocatalyst was measured in inert atmosphere (He) and after that, in presence of CO_2. The measurements were reproducibly repeated for each sample.

3.3.3. Photocatalytic NO_x Oxidation

For the NO_x oxidation measurements, a homemade flow-type setup was employed. The method is based on ISO/DIS 22197−1 standard and the procedure for evaluation of the photocatalytic NO oxidation is described in details in our previous work [48]. In brief, the powder samples were pressed in flat holders and placed in the photoreactor, where a gas with 1 ppm NO, humidity of 50%, was supplied with a constant flow rate of 3 L/min. Initially, a dark period of ~5 min was allowed. Then, the light was turned on and the concentrations of the NO, the formed NO_2 and the total NOx (NO + NO_2) were monitored by a Horiba APNA−370 chemiluminescence-based NO_x analyzer. After the light was turned off, the concentration of the NO in the gas flow returned to the initial concentration of 1 ppm. The photocatalytic activity of the materials was measured under UV-A irradiation (Philips Cleo Compact 15 W lamps) with intensity of 10 W/m^2 as well as under visible light irradiation (Nordex T5–8W–4000 K lamps, spectrum at Figure S7) with intensity of 7000 lx for 30 min.

It should be noted that for comparison reasons the activity of reference commercial TiO_2 photocatalyst Evonik-Degussa P25 was also measured in H_2 evolution, CO_2 reduction and NO_x oxidation at the same experimental conditions.

4. Conclusions

Bulk and exfoliated g-C_3N_4 were synthesized applying simple thermal treatment of non-covered precursor at 550 °C in air. The successive treatment at the same thermal conditions accompanied with a gradual decrease of the precursor mass resulted in g-C_3N_4 with graphene-like morphology and very high specific surface area of 513 m^2/g. The XRD patterns of the bulk and the exfoliated (1ex, 2ex and 3ex) g-C_3N_4 revealed gradual decrease of the interlayer distance from 0.323 nm (bulk) to 0.318 nm (3ex), whereas the increased delamination was confirmed by the TEM analysis. The light absorption was shifted to the UV region and the calculated band gap increased gradually from 2.7 to 3.04 eV. This blue shift was ascribed to quantum confinement effect caused by the high-level exfoliation. The electrochemical measurements showed that the conduction band potential was shifted to less negative values, while the valence band potentials were above (bulk and 1ex) and below (2ex and 3ex) the standard redox potential of ·OH formation. The EPR measurements demonstrated that the superoxide radicals ·O_2^- were the main reactive species formed under UV and visible light irradiation. Their gradual increase was ascribed to the large exposed surface and low e^--h^+ recombination. The photocurrent measurements suggested improved charge separation for sample 3ex.

The highly exfoliated g-C_3N_4 exhibited significant photocatalytic activity in H_2 evolution, CO_2 reduction and NO_x oxidation. In the H_2 evolution, the sample 3ex exhibited activity ~6 times higher than bulk under UV light and ~2 times higher under visible light. In the CO_2 reduction, the yields of CO, CH_4 and H_2 in presence of 3ex were almost 2, 3 and 8 times, respectively, higher than in case of bulk g-C_3N_4. In addition, the 2ex exhibited high selectivity towards CO_2 reduction reactions (CH_4 and CO formation), whereas the 3ex exhibited high selectivity for H_2 evolution. In the NO_x oxidation, the total NO_x removal by 2ex and 3ex under UV irradiation was ~4 and ~3 times, respectively, higher than bulk. Although less prominent, increase of the visible light activity was recorded despite the widening of the band gap. The results were related to the synergetic effect of the achieved large SSA and decreased e^--h^+ recombination. The graphene-like g-C_3N_4 proved very promising in photocatalytic CO_2 reduction and H_2 evolution.

XRD patterns of the g-C$_3$N$_4$ materials before and after photocatalytic activity tests in NO$_x$ oxidation; S5. FT-IR spectra of the g-C$_3$N$_4$ materials before and after photocatalytic activity tests in NO$_x$ oxidation; S6. Long-term (8 h) measurements for 3ex in H$_2$ evolution and 2ex in NO$_x$ oxidation.

Author Contributions: Conceptualization, N.T., K.K., and C.T.; investigation, N.T., I.P., T.G., N.I., N.B., P.D., M.E., and M.R.; resources, N.T., K.K., P.D., and C.T.; supervision, K.K. and C.T.; writing original draft, N.T. and K.K.; revision, N.T., I.P., T.G., K.K., and C.T. All authors have read and agreed to the published version of the manuscript.

Conflicts of Interest: The authors declare no conflict of interest.

References

1. Li, X.; Xiong, J.; Gao, X.; Huang, J.; Feng, Z.; Chen, Z.; Zhu, Y. Recent advances in 3D g-C$_3$N$_4$ composite photocatalysts for photocatalytic water splitting, degradation of pollutants and CO$_2$ reduction. *J. Alloys Comp.* **2019**, *802*, 196–209. [CrossRef]

2. Christoforidis, K.C.; Fornasiero, P. Photocatalytic Hydrogen production: A rift into the future energy supply. *Chem. Cat. Chem.* **2017**, *9*, 1523–1544. [CrossRef]

3. Fu, J.; Xu, Q.; Low, J.; Jiang, C.; Yu, J. Ultrathin 2D/2D WO$_3$/g-C$_3$N$_4$ step-scheme H$_2$-production photocatalyst. *Appl. Catal. B Environ.* **2019**, *243*, 556–565. [CrossRef]

4. Cao, S.; Yu, J. g-C$_3$N$_4$-Based Photocatalysts for Hydrogen Generation. *J. Phys. Chem. Lett.* **2014**, *5*, 2101–2107. [CrossRef]

5. Cheng, J.; Hu, Z.; Li, Q.; Li, X.; Fang, S.; Wu, X.; Li, M.; Ding, Y.; Liu, B.; Yang, C.; et al. Fabrication of high photoreactive carbon nitride nanosheets by polymerization of amidinourea for hydrogen production. *Appl. Catal. B Environ.* **2019**, *245*, 197–206. [CrossRef]

6. Shehzad, N.; Tahir, M.; Johari, K.; Murugesan, T.; Hussain, M. A critical review on TiO$_2$based photocatalytic CO$_2$reductionsystem: Strategiestoimprove efficiency. *J. CO$_2$ Util.* **2018**, *26*, 98–122. [CrossRef]

7. Abdullah, H.; Khan, M.M.R.; Ong, H.R.; Yaakob, Z. Modified TiO$_2$photocatalyst for CO$_2$ photocatalytic reduction: An overview. *J. CO$_2$ Util.* **2017**, *22*, 15–32. [CrossRef]

8. Lingampalli, S.R.; Ayyub, M.M.; Rao, C.N.R. Recent Progress in the Photocatalytic Reduction of Carbon Dioxide. *ACS Omega* **2017**, *2*, 2740–2748. [CrossRef]

9. Yang, C.; Tan, Q.; Li, Q.; Zhou, J.; Fan, J.; Li, B.; Sun, J.; Lv, K. 2D/2D Ti$_3$C$_2$MXene/g-C$_3$N$_4$nanosheetsheterojunction for high efficient CO$_2$ reduction photocatalyst: Dual effects of urea. *Appl. Catal. B Environ.* **2020**, *268*, 118738. [CrossRef]

10. Cao, S.; Low, J.; Yu, J.; Jaroniec, M. Polymeric Photocatalysts Based on Graphitic Carbon Nitride. *Adv. Mater.* **2015**, *27*, 2150–2176. [CrossRef]

11. Prasad, C.; Tang, H.; Bahadur, I. Graphitic carbon nitride based ternary nanocomposites: From synthesis to their applications in photocatalysis: A recent review. *J. Mol. Liq.* **2019**, *281*, 634–654. [CrossRef]

12. Shayegan, Z.; Lee, C.-S.; Haghighat, F. TiO$_2$photocatalyst for removal of volatile organic compounds in gas phase—A review. *Chem. Eng. J.* **2018**, *334*, 2408–2439. [CrossRef]

13. Fu, J.; Yu, J.; Jiang, C.; Cheng, B. g-C$_3$N$_4$-Based Hetero structured Photocatalysts. *Adv. Energy Mater.* **2017**, *1701503*, 1–31.

14. Kumar, S.; Karthikeyan, S.; Lee, A. g-C$_3$N$_4$-Based Nanomaterials for Visible Light-Driven Photocatalysis. *Catalysts* **2018**, *8*, 74. [CrossRef]

15. Ma, J.; Wang, C.; He, H. Enhanced photocatalytic oxidation of NO over g-C$_3$N$_4$-TiO$_2$ under UV and visible light. *Appl. Catal. B Environ.* **2016**, *184*, 28–34. [CrossRef]

16. Papailias, I.; Todorova, N.; Giannakopoulou, T.; Yu, J.; Dimotikali, D.; Trapalis, C. Photocatalytic activity of modified g-C$_3$N$_4$/TiO$_2$ nanocomposites for NO$_x$ removal. *Catalysis Today* **2017**, *280*, 37–44. [CrossRef]

17. Wen, J.; Xie, J.; Chen, X.; Li, X. A review on g-C$_3$N$_4$-based photocatalysts. *Appl. Surf. Sci.* **2017**, *391 Pt B*, 72–123. [CrossRef]

18. Ma, Y.; Liu, E.; Hu, X.; Tang, C.; Wan, J.; Li, J.; Fan, J. A simple process to prepare few-layer g-C$_3$N$_4$ nanosheets with enhanced photocatalytic activities. *Appl. Surf. Sci.* **2015**, *358*, 246–251. [CrossRef]

19. Papailias, I.; Todorova, N.; Giannakopoulou, T.; Ioannidis, N.; Boukos, N.; Athanasekou, C.P.; Dimotikali, D.; Trapalis, C. Chemical vs thermal exfoliation of g-C$_3$N$_4$ for NO$_x$ removal under visible light irradiation. *Appl. Catal. B Environ.* **2018**, *239*, 16–26. [CrossRef]

20. Dong, F.; Sun, Y.J.; Wu, L.W.; Fu, M.; Wu, Z. Facile transformation of low cost thiourea into nitrogen-rich graphitic carbon nitride nanocatalyst with high visible light photocatalytic performance. *Catal. Sci. Technol.* **2012**, *2*, 1332–1335. [CrossRef]

21. Li, Y.; Wang, M.-Q.; Bao, S.-J.; Lu, S.; Xu, M.; Long, D.; Pu, S. Tuning and thermal exfoliation graphene-like carbon nitride nanosheets for superior photocatalytic activity. *Ceramics Int.* **2016**, *42*, 18521–18528. [CrossRef]

22. Cheng, J.; Hu, Z.; Lv, K.; Wu, X.; Li, Q.; Li, Y.; Li, X.; Sun, J. Drastic promoting the visible photoreactivity of layered carbon nitride by polymerization of dicyandiamide at high pressure. *Appl. Catal. B Environ.* **2018**, *232*, 330–339. [CrossRef]

23. Han, D.; Liu, J.; Cai, H.; Zhou, X.; Kong, L.; Wang, J.; Shi, H.; Guo, Q.; Fan, X. High-yield and low-cost method to synthesize large-area porous g-C$_3$N$_4$ nanosheets with improved photocatalytic activity for gaseous nitric oxide and 2-propanol photodegradation. *Appl. Surf. Sci.* **2019**, *464*, 577–585. [CrossRef]

24. Papailias, I.; Giannakopoulou, T.; Todorova, N.; Dimotikali, D.; Vaimakis, T.; Trapalis, C. Effect of processing temperature on structure and photocatalytic properties of g-C$_3$N$_4$. *Appl. Surf. Sci.* **2015**, *358*, 278–286. [CrossRef]

25. Zhao, Z.; Sun, Y.; Luo, Q.; Dong, F.; Li, H.; Ho, W.-K. Mass-Controlled Direct Synthesis of Graphene-like Carbon Nitride Nanosheets with Exceptional High Visible Light Activity. Less is Better. *Sci. Rep.* **2015**, *5*, 14643. [CrossRef]

26. Zhu, K.; Lv, Y.; Liu, J.; Wang, W.; Wang, C.; Wang, P.; Meng, A.; Li, Z.; Li, Q. Explosive thermal exfoliation of intercalated graphitic carbon nitride for enhanced photocatalytic degradation properties. *Ceram. Int.* **2019**, *45*, 3643–3647. [CrossRef]

27. Wu, X.; Cheng, J.; Li, X.; Li, Y.; Lv, K. Enhanced visible photocatalytic oxidation of NO by repeated calcination of g-C$_3$N$_4$. *Appl. Surf. Sci.* **2019**, *465*, 1037–1046. [CrossRef]

28. She, X.; Wu, J.; Zhong, J.; Xu, H.; Yang, Y.; Vajtai, R.; Lou, J.; Liu, Y.; Du, D.; Li, H.; et al. Oxygenated monolayer carbon nitride for excellent photocatalytic Hydrogen evolution and external quantum efficiency. *Nano Energy* **2016**, *27*, 138–146. [CrossRef]

29. Niu, P.; Zhang, L.; Liu, G.; Cheng, H.-M. Graphene-Like Carbon Nitride Nanosheets for Improved Photocatalytic Activities. *Adv. Funct. Mater.* **2012**, *22*, 4763–4770. [CrossRef]

30. Zhao, H.; Yu, H.; Quan, X.; Chen, S.; Zhang, Y.; Zhao, H.; Wang, H. Fabrication of atomic single layer graphitic-C$_3$N$_4$ and its high performance of photocatalytic disinfection under visible light irradiation. *Appl. Catal. B Environ.* **2014**, *152–153*, 46–50. [CrossRef]

31. Song, X.; Yang, Q.; Jiang, X.; Yin, M.; Zhou, L. Porous graphitic carbon nitride nanosheets prepared under self-producing atmosphere for highly improved photocatalytic activity. *Appl. Catal. B Environ.* **2017**, *217*, 322–330. [CrossRef]

32. Zhu, B.; Xia, P.; Ho, W.K.; Yu, J.G. Isoelectric point and adsorption activity of porous g-C$_3$N$_4$. *Appl. Surf. Sci.* **2015**, *344*, 188–195. [CrossRef]

33. Cao, Y.; Lia, Q.; Wang, W. Construction of a crossed-layer-structure MoS$_2$/g-C$_3$N$_4$ heterojunction with enhanced photocatalytic performance. *RSC Adv.* **2017**, *7*, 6131–6139. [CrossRef]

34. Jürgens, B.; Irran, E.; Senker, J.; Kroll, P.; Müller, H.; Schnick, W. Melem (2,5,8-triamino-tri-s-triazine), an important intermediate during condensation of melamine rings to graphitic carbon nitride: Synthesis, structure determination by X-ray powder diffraction, solid-state NMR, and theoretical studies. *J. Am. Chem. Soc.* **2003**, *125*, 10288–10300. [CrossRef] [PubMed]

35. Thomas, A.; Fischer, A.; Goettmann, F.; Antonietti, M.; Mueller, J.O.; Schloegl, R.; Carlsson, J.M. Graphitic carbon nitride materials: Variation of structure and morphology and their use as metal-free catalysts. *J. Mater. Chem.* **2008**, *18*, 4893–4908. [CrossRef]

36. Dong, F.; Wu, L.W.; Sun, Y.J.; Fu, M.; Wu, Z.B.; Lee, S.C. Efficient synthesis of polymeric g-C$_3$N$_4$ layered materials as novel efficient visible light driven photocatalysts. *J. Mater. Chem.* **2011**, *21*, 15171–15174. [CrossRef]

37. Yuan, X.; Zhou, C.; Jin, Y.; Jing, Q.; Yang, Y.; Shen, X.; Tang, Q.; Mu, Y.; Du, A.-K. Facile synthesis of 3D porous thermally exfoliated g-C$_3$N$_4$ nanosheet with enhanced photocatalytic degradation of organic dye. *J. Colloid Interface Sci.* **2016**, *468*, 211–219. [CrossRef]

38. Nosaka, Y.; Nosaka, A.Y. Identification and roles of the active species generated on various photocatalysts. In *Photocatalysis and Water Purification: From Fundamentals to Recent Applications*; Pichat, P., Ed.; Wiley-VCH: Weinheim, Germany, 2013; pp. 3–24.

39. Brezova, V.; Gabcova, S.; Dvoranova, D.; Stasko, A. Reactive oxygen species produced upon photoexcitation of sunscreens containing titanium dioxide (An EPR study). *J. Photochem. Photobiol. B Biol.* **2005**, *79*, 121–134. [CrossRef]

40. Toumazatou, A.; Antoniadou, M.; Sakellis, E.; Tsoutsou, D.; Gardelis, S.; Romanos, G.E.; Ioannidis, N.; Boukos, N.; Dimoulas, A.; Falaras, P.; et al. Boosting visible light harvesting and charge separation in surface modified TiO$_2$ photonic crystal catalysts with CoO$_x$ nanoclusters. *Mater. Adv.* **2020**. [CrossRef]

41. Dvoranová, D.; Mazúr, M.; Papailias, I.; Giannakopoulou, T.; Trapalis, C.; Brezová, V. EPR Investigations of G-C$_3$N$_4$/TiO$_2$ Nanocomposites. *Catalysts* **2018**, *8*, 47. [CrossRef]

42. Schneider, J.; Bahnemann, D.W. Undesired Role of Sacrificial Reagents in Photocatalysis. *J. Phys. Chem. Lett.* **2013**, *4*, 3479–3483. [CrossRef]

43. Papailias, I.; Todorova, N.; Giannakopoulou, T.; Ioannidis, N.; Dallas, P.; Dimotikali, D.; Trapalis, C. Novel torus shaped g-C$_3$N$_4$ photocatalysts. *Appl. Catal. B Environ.* **2020**, *268*, 118733. [CrossRef]

44. Chang, F.; Zhang, J.; Xie, Y.; Chen, J.; Li, C.; Wang, J.; Luo, J.; Deng, B.; Hu, X. Fabrication, characterization, and photocatalytic performance of exfoliated g-C$_3$N$_4$–TiO$_2$ hybrids. *Appl. Surf. Sci.* **2014**, *311*, 574–581. [CrossRef]

45. Zang, M.; Shi, L.; Liang, L.; Li, D.; Sun, J. Heterostructured g-C$_3$N$_4$/Ag–TiO$_2$ composites with efficient photocatalytic performance under visible-light irradiation. *J. RSC Adv.* **2015**, *5*, 56136–56144. [CrossRef]

46. Koci, K.; Reli, M.; Kozak, O.; Lacny, Z.; Placha, D.; Praus, P.; Obalova, L. Influence of reactor geometry on the yield of CO$_2$ photocatalytic reduction. *Catal. Today* **2011**, *176*, 212–214. [CrossRef]

47. Tasbihi, M.; Koci, K.; Edelmannova, M.; Troppova, I.; Reli, M.; Schomacker, R. Pt/TiO$_2$ photocatalysts deposited on commercial support for photocatalytic reduction of CO$_2$. *J. Photochem. Photobiol. A Chem.* **2018**, *366*, 72–80. [CrossRef]

48. Todorova, N.; Giannakopoulou, T.; Karapati, S.; Petridis, D.; Vaimakis, T.; Trapalis, C. Composite TiO$_2$/clays materials for photocatalytic NO$_x$ oxidation. *Appl. Surf. Sci.* **2014**, *319*, 113–120. [CrossRef]

49. Ou, M.; Wan, S.; Zhong, Q.; Zhang, S.; Song, Y.; Guo, L.; Cai, W.; Xu, Y. Hierarchical Z-scheme photocatalyst of g-C$_3$N$_4$@Ag/BiVO$_4$ (040) with enhanced visible-light-induced photocatalytic oxidation performance. *Appl. Catal. B Environ.* **2018**, *221*, 97–107. [CrossRef]

50. Dong, F.; Li, Q.; Sun, Y.; Ho, W.K. Noble metal-like behavior of plasmonic Bi particles as a cocatalyst deposited on (BiO)$_2$CO$_3$ microspheres for efficient visible light photocatalysis. *ACS Catal.* **2014**, *4*, 4341–4350. [CrossRef]

51. Giannakopoulou, T.; Papailias, I.; Todorova, N.; Boukos, N.; Liu, Y.; Yu, J.; Trapalis, C. Tailoring the energy band gap and edges' potentials of g-C$_3$N$_4$/TiO$_2$ composite photocatalysts for NO$_x$ removal. *Chem. Eng. J.* **2017**, *310*, 571–580. [CrossRef]